Final Draft
of the original manuscript:

Pirondi, A.; Bonara, N.; Steglich, D.; Brocks, W.; Hellmann, D.:
Simulation of failure under cyclic plastic loading by damage models
In: International Journal of Plasticity (2006) Elsevier

DOI: 10.1016/j.ijplas.2006.03.007

SIMULATION OF FAILURE UNDER CYCLIC PLASTIC LOADING BY DAMAGE MODELS

Pirondi[1,*], A., Bonora[2], N., Steglich, D.[3], Brocks, W.[3], Hellmann, D.[3]
[1]*DII - University of Parma, Parma, Italy*
[2]*DiMSAT – University of Cassino, Cassino, Italy*
[3]*GKSS Forschungszentrum, Geesthacht, Germany*

ABSTRACT
The purpose of this work is to simulate the evolution of ductile damage and failure involved by plastic strain reversals using damage models based on either Continuum Damage Mechanics (CDM) or porosity evolution. A low alloy steel for pressure vessels (20MnMoNi55) was chosen as reference material. The work includes both experimental and simulation phases. The experimental campaign involves different kinds of specimens and testing conditions. First, monotonic tensile tests have been performed in order to evaluate tensile and ductile damage behaviour. Then, the cyclic yielding behaviour has been characterized performing cyclic plasticity tests on cylindrical bars. Finally, cyclic loading tests in the plastic regime have been made on different Round Notched Bars (RNBs) to study the evolution of plastic deformation and damage under multiaxial stress conditions. The predictions of the different models were compared in terms of both, the specimens macroscopic response and local damage. Special emphasis was laid on predictions of the number of cycles prior to final failure and the crack initiation loci.

KEYWORDS: *cyclic plasticity, damage, porous metal plasticity, Continuum Damage Mechanics (CDM)*

NOTATION

a_{ij}	internal variable for kinematic hardening
b	isotropic hardening exponent
d_{ij}	Eulerian strain rate tensor
$h^{(\alpha)}$	internal variables for isotropic hardening
q	stress deviator related part of the yield function
$q_1; q_2; q_3$	parameters of the GTN and LPD models
p	hydrostatic stress related part of the yield function
C	kinematic hardening modulus
D	damage variable in PB model
D_0	initial damage in PB model
D_{cr}	critical damage in PB model
E_0	Young's modulus of undamaged material
E	effective (damaged) Young's modulus
$H\langle\ \rangle$	step function
f	void volume fraction
f_c	critical void volume fraction

* Corresponding author: Dipartimento di Ingegneria Industriale - Università di Parma, Parco Area delle Scienze 181/A, 43100 Parma, Italy. Tel.: 0039-0521-905885. Fax: 0039-0521-905705. e-mail: pirondia@me.unipr.it

f^*	damage variable in GTN and LPD
R_ε	ratio of minimum to maximum strain of the cycle
R_δ	ratio of minimum to maximum displacement of the cycle
R	current radius of the yield surface
R_0	initial yield stress (zero plastic strain)
R_∞	saturated radius of the yield surface
x_{ij}	backstress tensor
x'_{ij}	backstress tensor deviator
α	damage exponent
ε_{ij}	strain tensor
ε_{ij}^{el}	elastic strain tensor
ε_{ij}^{pl}	plastic strain tensor
ε_{cr}	theoretical failure strain under uniaxial state of stress (PB model)
ε_{max}	maximum strain of the cycle
ε_{min}	minimum strain of the cycle
ε_f	failure strain measured in a tensile test
ε_{th}	damage threshold strain (uniaxial)
ε_{eq}^{pl}	accumulated equivalent plastic strain
γ	kinematic hardening exponent
κ	damage acceleration parameter
λ	plastic multiplier
ρ	radius of curvature of the neck in a tensile test
σ_{eq}	equivalent von Mises stress
σ_{ij}	Cauchy stress tensor
σ'_{ij}	Cauchy stress tensor deviator
σ_m	mean stress
σ_y	yield strength
σ_u	ultimate stress
ν	Poisson's ratio
Φ	yield function

1. INTRODUCTION

The micromechanical approach to material failure has received considerable attention in the last two decades as a suitable alternative to more traditional methodologies. Its application has been so far mainly focused on the prediction of ductile failure in metals and alloys, which is known to be the result of microvoid nucleation from inclusions such as carbides and sulfides, their growth and coalescence due to plastic deformation. The modelling of this process at the mesoscale is the basis for the prediction of ductile failure in macroscopic components and structures. Many models have been developed since the initial studies of McClintock (1968) and Rice and Tracey (1969). They can be classified into three main classes: i) abrupt failure criteria, ii) porous metal plasticity, and iii) continuum damage mechanics (CDM). In the first group, failure is predicted when a micromechanical variable, for instance the cavity volume fraction (Rice and Tracey (1969), reaches a critical value characteristic of the material. In the second group, damage effects are accounted for into the plastic potential by a softening term, which is usually related to the void volume fraction in the material, see Gurson (1977), Needleman and Rice (1978), Tvergaard and Needleman (1984), Rousselier (1987). More recently, a number of unit cell based finite element studies have been performed in order to correlate void evolution and interaction with the resulting mesoscale material yield function. The role of void size was recently investigated in Tvergaard and Niordson (2004) using a non-local plasticity model proposed by Acharya and Bassani (2000), in Wen et al. (2005) incorporating void size into the Gurson model based on the Taylor dislocation model and in Li and Huang (2005) and Huang and Li (2005) as a boundary value problem.

Schacht *et al.* (2003) used the 3D voided unit cell to investigate the role and the effects associated with the crystallographic orientation of the matrix material, finding a substantial dependency of growth and coalescence on the anisotropy of the material surrounding the voids. Bonfoh *et al*. (2004) used porous metal plasticity to model damage evolution initiated by secondary included particles debonding in a polycrystalline material. The model developed by Gurson, Tvergaard and Needleman (Tvergaard and Needleman (1984))(GTN model) is extensively used to study ductile failure and crack propagation (Xia and Shih, 1995, Brocks *et al.*, 1996, Manhken, 2002, Besson *et al.*, 2003, Negre *et al.*, 2004, Yuan and Chen, 2004).

The CDM approach, initially proposed by Lemaitre (1985), considers instead the effects associated to a given damage condition through the definition of a thermodynamic state variable. Damage affects not only the yield function but also reduces the stiffness through the definition of the effective stress. Relative to the initial framework proposed by Lemaitre, several damage models using special expressions for the damage dissipation potential, have been derived and validated experimentally by various authors (Chandrakanth and Pandey (1993), Bonora (1997a,b), Tay and Yang (1986), Tay, (1990), Lin *et al*. (2004), Bonora *et al*. (2005)). More recently, a number of so-called non-local theories have been proposed (Fleck *et al.*, 1994, Fleck and Hutchinson, 1997, Bamman *et al.*, 1999). Anisotropic damage evolution was considered in Brünig, (2003), Brünig and Ricci (2005) and Menzel *et al.* (2005) while Voyidajis *et al.* (2004) developed a coupled non-local viscoplasticity and a non-local viscodamage model using the Kachanov damage definition. Lammer and Tsamakis (2000) compared different CDM models with reference to homogeneous and inhomogeneous deformations providing a formulation generalization to finite deformation.

However, engineering components and structures are typically subjected to cyclically varying loading conditions, which can eventually force the material to undergo cyclic plastic flow. The accumulation of plastic deformation with the number of cycles is a source of damage that, sooner or later, will lead to material failure. Damage is related to the irreversible processes that occur in the microstructure, therefore its presence affects the material constitutive response at meso/macro scale. Examples of conditions where plastic strain reversals may occur are earthquake loadings, cyclic overloads and the reeling of pipelines. Under cyclic plastic loading, different irreversible microstructural changes take place. At the lower amplitudes, persistent slip bands and rearrangement of dislocation systems into cell structures are the mechanisms that lead to low-cycle fatigue failure by crack initiation at grain boundaries (Klesnil and Lukas (1980); Polak (1991)). At the higher amplitudes, quasi-static failure due to void nucleation and growth at the secondary phase inclusions occur, for which very short lives are expected.
Still little attention has been given to the possibility of incorporating damage into cyclic plasticity by means of micromechanics. Recent works regarding porous metal plasticity are the ones of Leblond *et al.* (1995) as well as Besson and Guillemer-Neel (2003) who introduced nonlinear kinematic hardening into the GTN-model. Cedergren et al. (2004) used a similar formulation but included viscoplasticity to simulate the behaviour of a powder metallurgy steel.
As far as CDM is concerned, Pirondi and Bonora (2003) extended the nonlinear CDM model of Bonora (1997) to tension-compression loading introducing unilateral conditions in the evolution of damage and plastic strain. Even more recently, in Xiao (2004) fatigue and creep damage were modelled by coupling two separate damage variables, and Yang and Nasser (2004) and Gomez and Basaran (2005) developed a coupled damage- viscoplastic constitutive model to study failure of solder joints in surface-mount integrated circuits. The relationship between damage models of the CDM and porous metal plasticity group is illustrated by Steglich *et al.* (2005) using unit cell models.
The limited experience in the application of micromechanics to cyclic plasticity failure leaves the issue of transferability of the models between different stress states (i.e. triaxialities) virtually unexplored. In Pirondi and Bonora (2003) a good correlation was found between a cyclic plasticity loading experiment conducted on a Round Notched Bar (RNB) and the corresponding simulation with a CDM model.
The present paper is devoted to the extension of the experience made in Pirondi and Bonora (2003) in order to assess the predictive capabilities of micromechanical models based on either porosity evolution or CDM. In particular, the models of Leblond *et al.* (1995) (LPD model) and of Pirondi and Bonora (2003) (PB model) are considered for the two categories, respectively. A low alloy steel for pressure vessels (20MnMoNi55) is chosen as reference for this study. The work includes both experimental and simulation phases. The experimental campaign involves different kinds of specimens and testing conditions:

i) Monotonic tensile tests to evaluate tensile and ductile damage behaviour. The aim of these experiments is also to calibrate the damage parameters.
ii) Cyclic plasticity tests on cylindrical specimens to characterise uniaxial cyclic yielding behaviour.
iii) Cyclic plasticity tests on Round Notched Bars (RNBs) with different diameter/notch radius ratios to study plasticity and failure evolution under multiaxial stress conditions.

The calibration of damage parameters based on tensile tests was performed since a well-established procedure is available in this case (Bernauer and Brocks (2002), Bonora et al. (2004)). The underlying assumption is that failure under cyclic plastic loading is a result of void nucleation, growth and coalescence process, too, as it may occur for very high plastic strain amplitudes and/or triaxialities.
The contribution concerns the comparison of the experiments on RNBs with the results of CDM and porosity models in terms of both, the specimens' macroscopic response and local damage evolution. Special emphasis is laid on predictions of the number of cycles prior to final failure and the crack initiation loci.

2. MODELLING

Axisymmetric FE models of the specimen geometries described in the next chapter are developed using 4-noded, fully integrated elements. Since stress gradients occurring in the presently used test samples are relatively small, linear elements were chosen to capture enough details of the stress distribution and reduce computational burden at the same time. Symmetry conditions are imposed in order to model only one quarter of the geometry. The mesh is built up in order to have an element dimension of about 0.1mm in the region where failure is expected to occur, which is the typical dimension of a RVE in metals (Lemaitre (1996)). In this way it is possible to define mesocrack initiation when the first element attains critical damage at all of its integration points. The simulations are run using ABAQUS v.6.3 software with subroutines specifically developed for the micromechanical models. The constitutive framework, micromechanical models and cyclic yielding behaviour are described below.

2.1 Rate independent plasticity framework

Inelastic deformations are described in the framework of the classical theory of rate-independent plasticity. The yield function has the general form

$$\Phi\left(q, p, h^{(\alpha)}\right) \le 0\,; \quad q = \sqrt{\tfrac{3}{2} s'_{ij} s'_{ij}}\,, \quad p = -\tfrac{1}{3} s_{kk}\,, \tag{1}$$

s'_{ij} denoting the deviatoric part of the tensor s_{ij}. The dependence of Φ on p vanishes for incompressible plastic deformations, but appears in pressure-dependent plasticity. The difference between Cauchy stresses, σ_{ij}, and back stresses, x_{ij}, for kinematic hardening,

$$s_{ij} = \sigma_{ij} - x_{ij}\,, \tag{2}$$

is used. The scalar quantities $h^{(\alpha)}$ denote internal variables for isotropic hardening or softening. The (symmetric) strain rate deformation tensor is decomposed in an elastic and a plastic contribution,

$$d_{ij} = d_{ij}^{el} + d_{ij}^{pl}\,, \tag{3}$$

which is equivalent to the multiplicative decomposition of the respective displacement gradients for small elastic strains. Hooke's law is assumed for elastic deformation rates and Jaumann stress rates according to the Hughes and Winget (1980) approach

$$\overset{\nabla}{\sigma}_{ij} = C_{ijkl} d_{ij}^{el} = C_{ijkl}\left(d_{ij} - d_{ij}^{pl}\right). \tag{4}$$

An associated flow (or normality) rule

$$d_{ij}^{pl} = \dot{\lambda} \frac{\partial \Phi}{\partial \sigma_{ij}} = \dot{\lambda}\left(\frac{\partial \Phi}{\partial q} n_{ij} - \frac{1}{3}\frac{\partial \Phi}{\partial p}\delta_{ij}\right) = \dot{e}_q n_{ij} + \frac{1}{3}\dot{e}_p \delta_{ij}\;; \qquad \text{with} \qquad n_{ij} = \dot{\lambda}\frac{3 s_{ij}}{2q} \tag{5}$$

is postulated for the plastic deformation rates. The two scalar variables, $\dot{e}_q$ and $\dot{e}_p$, denoting deviatoric and dilatoric strain rates as introduced by Aravas (1987), have to satisfy the condition

$$\dot{e}_p \frac{\partial \Phi}{\partial q} + \dot{e}_q \frac{\partial \Phi}{\partial p} = 0 , \tag{6}$$

which derives from eliminating the plastic multiplier, $\dot{\lambda}$.
Finally, evolution equations for the internal variables of isotropic and kinematic hardening,

$$\left.\begin{aligned} \dot{h}^{(\alpha)} &= g\left(\varepsilon_{ij}^{pl}, s_{ij}, h^{(\alpha)}\right) \\ \overset{\nabla}{a}_{ij} &= F_{ij}\left(\varepsilon_{ij}^{pl}, s_{ij}, h^{(\alpha)}\right) \end{aligned}\right\} \tag{7}$$

complete the constitutive relations. Strain hardening materials contain a single scalar hardening variable, the accumulated equivalent plastic strain,

$$\varepsilon_{eq}^{pl} = \int_0^t \sqrt{\tfrac{2}{3} d_{ij}^{pl} d_{ij}^{pl}}\, d\tau , \tag{8}$$

determining the current flow stress by a material dependent relation $R(\varepsilon_{eq}^{pl})$.

2.2 Damage models

Leblond-Perrin-Devaux (LPD). The damage models are formulated in the framework of the theory of rate-independent, but pressure-dependent plasticity. Models of ductile damage include (at least) one additional internal variable - besides the accumulated equivalent plastic strain, ε^{pl}_{eq}, for isotropic and back stresses, x_{ij}, for kinematic hardening - which is identical to or depends on the void-volume fraction, f. The latter is defined as the ratio of the volume of all cavities in a material element to its total volume. An evolution equation holds for the void-volume fraction, consisting of a void growth and a void nucleation part, in general,

$$\dot{f} = \dot{f}_{\text{growth}} + \dot{f}_{\text{nucl}} \quad \text{with} \quad f(t_0) = f_0 \ . \tag{9}$$

The growth term is obtained from the conservation of mass,

$$\dot{f}_{growth} = (1 - f) d_{kk}^{pl} , \tag{10}$$

and the nucleation term is commonly adopted from an empirical approach by Chu and Needleman (1980) assuming a normal distribution of void nucleating particles:

$$\dot{f}_{nucl} = A \dot{\varepsilon}_{eq}^{pl} = \frac{f_N}{s_N \sqrt{2\pi}} \exp\left[-\frac{1}{2} \left(\frac{\varepsilon_{eq}^{pl} - \varepsilon_N}{s_N} \right)^2 \right] \tag{11}$$

From eqns. (13) and (14) it turns out that negative void accumulation is obtained for negative strain rates. The various models proposed in this context differ mainly by the yield function, eqn. (1). The yield function of the so-called GTN model,

$$\Phi = \frac{3 \sigma'_{ij} \sigma'_{ij}}{2\left[R\left(\varepsilon_{eq}^{pl}\right)\right]^2} + 2 q_1 f^* \cosh\left(q_2 \frac{\sigma_{kk}}{2 R\left(\varepsilon_{eq}^{pl}\right)} \right) - \left(1 + q_3 f^{*2}\right) = 0 , \tag{12}$$

has originally been derived from micromechanical considerations by Gurson (1977). The modifications by Needleman and Tvergaard (1984); Tvergaard and Needleman

(1984) concern the introduction of three additional material parameters, q_i (i = 1, 2, 3), affecting the yield behaviour and the damage variable, f^*, which equals the void-volume fraction, f, up to a critical value, f_c, for beginning coalescence of voids, beyond which damage is accelerated by a factor $\kappa > 1$,

$$f^* = \begin{cases} f & \text{for} \quad f \le f_c \\ f_c + \kappa(f - f_c) & \text{for} \quad f > f_c \end{cases}. \quad (13)$$

The GTN model accounts for isotropic hardening only, which limits its application to monotonous loading, in principle. Leblond, Perrin, Devaux (1995) have extended Gurson's yield function to kinematic hardening by replacing the Cauchy stress tensor by the difference of Cauchy stress and backstress tensor, eqn. (2), which leads to the yield function

$$\Phi = \frac{3 s'_{ij} s'_{ij}}{2\bar{\sigma}_1^{\,2}} + 2 q_1 f^* \cosh\left(q_2 \frac{s_{kk}}{2\bar{\sigma}_2} \right) - \left(1 + q_3 f^{*2} \right) = 0 . \quad (14)$$

The quantities $\bar{\sigma}_1$, $\bar{\sigma}_2$ result from a re-calculation of the homogenisation problem for hardening material. The numerical implementation used here is described in Mühlich and Brocks (2003).

Pirondi-Bonora (PB). In Bonora (1997a) the material yield function was written as:

$$\Phi(s_{ij}, R, x_{ij}) = q - f(R, x_{ij}, D) = 0 , \quad (15)$$

being $f(R,x_{ij};D)$ the experimentally determined material flow curve, where the effects of backstress are considered through a quadratic term as usual. The dependence on D is implicit in the sense that it someway affects the yield properties but it is experimentally not possible to separate the hardening effect due to plastic deformation from the softening effect induced by damage evolution. Therefore, no softening effect appears explicitly in the material yield function.

In this model, the damage evolution law was nonlinear in the accumulated plastic strain:

$$\dot{D} = \alpha \cdot \frac{\left(D_{cr} - D_0 \right)^{\frac{1}{\alpha}}}{ln(\varepsilon_{cr} / \varepsilon_{th})} \cdot f\left(\frac{\sigma_m}{\sigma_{eq}} \right) \cdot \left(D_{cr} - D \right)^{\frac{\alpha - 1}{\alpha}} \cdot \frac{\dot{\varepsilon}_{eq}^{pl}}{\varepsilon_{eq}^{pl}} \quad (16)$$

Pirondi and Bonora (2003) extended the formulation to the case of cyclic plastic loading according to the following hypotheses:

i) Damage accumulates and its effect on material stiffness is active if and only if stress triaxiality (the ratio of mean stress, $\sigma_m = 1/3 \sigma_{kk}$, and the equivalent stress, $\sigma_{eq} = (3/2 \sigma'_{ij} \sigma'_{ij})^{0.5}$) is positive, that is:

$$\text{if } \sigma_m / \sigma_{eq} \ge 0 \text{ and } \varepsilon \ge \varepsilon_{th} \mapsto \dot{D} > 0 , \; D \ne 0 \text{ and } E = E_0 (1 - D) \quad (17)$$

ii) Under compressive state of stress (i.e. $\sigma_m / \sigma_{eq} < 0$) damage does not accumulate and its effects are inactive, so:

$$\text{if } \sigma_m / \sigma_{eq} < 0 \text{ and } D > 0 \mapsto \quad \dot{D} = 0 \text{ and } E = E_0 . \quad (18)$$

The complete set of constitutive equations can be written as follows:

$$\varepsilon_{ij}^{el} = \frac{1 + \nu}{E} \frac{\sigma_{ij}}{1 - D} - \frac{\nu}{E} \frac{\sigma_{kk}}{1 - D} \delta_{ij} \quad (19)$$

$$d_{ij}^{pl} = \dot{\lambda} \frac{\partial \Phi}{\partial \sigma_{ij}} = \frac{3}{2} \dot{\lambda} \frac{s'_{ij}}{s_{eq}} \quad (20)$$

$$\dot{a}_{ij} = -\dot{\lambda}\frac{\partial \Phi}{\partial x'_{ij}} = d^{pl}_{ij} - \frac{3}{2X_\infty} x'_{ij}\dot{\lambda} \qquad (21)$$

$$\dot{h} = -\dot{\lambda}\frac{\partial \Phi}{\partial R} = \dot{\lambda} = \varepsilon_{eq}{}^{pl} \qquad (22)$$

$$\dot{D}^{+} = \alpha \cdot \frac{\left(D_{cr} - D_0\right)^{\frac{1}{\alpha}}}{ln(\varepsilon_{cr} / \varepsilon_{th})} \cdot f\left(\frac{\sigma_m}{\sigma_{eq}}\right) \cdot \left(D_{cr} - D^{+}\right)^{\frac{\alpha-1}{\alpha}} \cdot \frac{\dot{\varepsilon}^{pl+}_{eq}}{\varepsilon^{pl+}_{eq}} \qquad (23)$$

$$f\left(\frac{\sigma_m}{\sigma_{eq}}\right) = \frac{2}{3}\left(1+\nu\right) + 3\left(1-2\nu\right)\left(\frac{\sigma_m}{\sigma_{eq}}\right)^2 \qquad (24)$$

$$\dot{\varepsilon}^{pl+}_{eq} = \dot{\lambda} \cdot H\left\langle \sigma_m / \sigma_{eq} \right\rangle \qquad (25)$$

$$E = E_0(1 - D^{+})H\left\langle \sigma_m / \sigma_{eq} \right\rangle \qquad (26)$$

where

$$H\left\langle \sigma_m / \sigma_{eq} \right\rangle = \begin{cases} 0 & \sigma_m / \sigma_{eq} < 0 \\ 1 & \sigma_m / \sigma_{eq} \geq 0 \end{cases} . \qquad (27)$$

The superscript "+" indicates quantities increasing only if triaxiality is positive. ε^{pl+}_{eq} is obtained by time integration of Eqn. (25).

2.3 Cyclic yielding behaviour

The cyclic hardening behaviour is described with the model of Chaboche (1989), which combines a nonlinear kinematic and isotropic hardening. An analytical relation with an initial yield stress, R_0, and a saturation value, R_∞, is applied for the isotropic flow stress,

$$R = R_0 + \left(R_\infty - R_0\right)\left(1 - e^{-b\varepsilon^{pl}_{eq}}\right), \qquad (28)$$

and an extension of Ziegler's law with an additional recall-term for the evolution of backstress

$$\dot{x}_{ij} = \frac{C}{R} s_{ij}\dot{\varepsilon}^{pl}_{eq} - \gamma x_{ij}\dot{\varepsilon}^{pl}_{eq} . \qquad (29)$$

where differently from linear kinematic hardening (Ziegler's law) R is not constant but comes from eqn. (28) as a function of plastic strain. This model allows to reproduce most of the features of the cyclic plastic behaviour such as Bauschinger effect, cyclic hardening or softening, ratchetting of strain under constant stress amplitude and relaxation of mean stress.

3. EXPERIMENTS

The material under consideration is a German low alloy steel 20MnMoNi55 (similar to A508 in the US designation). The specimens have been extracted from a homogenous piece of the bottom section of a nuclear pressure vessel. The material composition is given in Table 1.

3.1 Tensile tests on Round Bars (RB)

Tensile tests were performed according to the italian UNI 6380-68 standard prescriptions. with the following purposes:

- Determination of the yield strength and hardening behaviour (true stress -- true strain curves) using Bridgman correction.
- Verification of the micromechanical models.

For the application of Bridgman correction, the profile of the neck was monitored during the test by digital image acquisition. The neck profile is a further option to verify the calibration of the models. In this case, necking should be forced to occur in the middle of the gauge length by introducing a local small diameter reduction.
The specimen dimensions are shown in Fig. 1 for two different diameters, namely 5 and 10mm. The tests were performed under displacement control. The measurement of the strain before necking was made with a 50mm gauge length extensometer.

3.2 Tensile tests on Flat Rectangular Hourglass specimens (FRHG)

The aim of this experiment was to evaluate tensile damage evolution and tune the parameters of the CDM model of Pirondi and Bonora (2003). The specimen is shown in Fig. 2. The slight hourglass shape was chosen to concentrate strain and therefore damage on a well determined section. The tests had to be run under displacement control. A series of partial unloadings was performed to evaluate the decrease of elastic modulus for increasing plastic strain, hence the damage as $D = 1 - E/E_0$. The elastic modulus was evaluated at the minimum section by means of a strain gauge. Further details on the experimental procedure can be found in Bonora et al. (2004).

3.3 Cyclic plasticity tests on cylindrical specimens (Damage Low Cycle, DLC)

This test was aimed at characterizing the cyclic flow curve. The specimen dimensions were taken from the ASTM E 606 standard test method for strain-controlled fatigue testing, with the only modifications of: i) a shorter gauge length to prevent buckling due to high compression straining and ii) flattening of the end for mounting into the available flat wedge grips (Fig. 3). The experiments were strain-range controlled using a 10mm gauge length extensometer. One specimen for each strain range was tested (companion samples method). A triangular waveshape symmetric cycle (R_ε=-1) was imposed with a strain rate of $10^{-3}s^{-1}$.

3.4 Cyclic plasticity tests on Round Notch Bars (RNBs)

Cyclically loaded round notch tensile bars represent the reference tests to verify the predictive performance of micromechanical models under proportional loading conditions. Two different mechanical situations were investigated by testing specimens with the same diameter of the notched section (8mm) but notch radius of 2mm (higher triaxiality) and 10mm (lower triaxiality), respectively. Preliminary numerical investigations Bonora et al. (1996) showed that the stress triaxiality distribution across the minimum section depends on the notch radius/section diameter r/d ratio and on the hardening exponent of the material, but it is fairly unaffected by the deformation level. Besides, for a notch radius not smaller than 2 mm the plastic strain distribution can still be regarded as uniform. The RNB geometries tested are given in Figs. 4 (RNB2) and 5 (RNB10).

The tests were conducted in a servohydraulic testing machine under displacement-controlled condition with a ratio of minimum to maximum displacement of -1 and a frequency of 0.004 Hz for notch radius R=2mm and 0.008 Hz for notch radius R=10mm. Five specimens for each notch radius were tested with different displacement range levels. The cycle amplitude was controlled by means of a 25mm-gauge length clip gauge placed across the notch. The change of the diameter in the notch was also monitored using a clip gauge. Load versus deflection hysteresis loops were recorded during the tests.

4. PARAMETER CALIBRATION

4.1 Hardening behaviour

Tensile loading. Five RB specimens were tested for each diameter. The stress-strain data are characterized by a yield plateau followed by a moderate hardening ($\sigma_u/\sigma_y \cong 1.28$). From the tests, the tensile mechanical properties were evaluated as: $\sigma_y = 472$MPa, $\sigma_u = 602$MPa, $\varepsilon_f = 22.8\%$. The elastic constants were assumed to be $E = 204$GPa and $\nu = 0.3$, respectively. Monitoring of the necking phase by digital image acquisition allowed to calculate true stres-true strain data and to operate Bridgman correction as reported in Pugh (1970):

$$\sigma_B = \frac{\sigma_{true}}{\left(1 + 2\frac{\rho}{a}\right) * Log\left(1 + \frac{a}{2\rho}\right)} \quad (29)$$

The cross section radius a has been determined from the images using a pixel-count algorithm while the calculation of the curvature radius ρ was performed after fitting the profile with a second-order polynomial. The results are shown in Fig.6.

Cyclic loading. DLC specimens were tested at symmetric strain amplitudes $\varepsilon_a = \Delta\varepsilon/2 = (\varepsilon_{max} - \varepsilon_{min})/2$ of 1.5, 2 and 2.5%, respectively. The corresponding stabilized cycles are shown in Fig. 7. The tips of the stabilized cycles are compared in Fig. 8 with the corresponding peak values (obtained after N=2 cycles) and with the tensile stress-strain data. The cyclic behaviour is characterized by an initial rapid cyclic hardening followed by softening for all of the strain ranges tested, while a modest hardening with respect to the tensile behaviour is recorded only for $\varepsilon_a = 2\%$.

The cyclic yielding model parameters, namely R_0, R_∞, b, C, γ, have been inferred in different ways for the LPD ad PB models, respectively. In the case of the LPD model, since failure is modelled as a progressive shrinking of the yield surface due to the increase of void volume fraction with the numbers of cycles, the parameters have been determined from the first 10 loading cycles, where the material showed cyclic strain hardening. The underlying assumption was that the softening exhibited after the first cycles could be modelled as a result of damage (i.e. void volume fraction) accumulation. The parameters are tuned by comparing FE simulations with the experimental response at $\Delta\varepsilon$=5%. The best fit was found with $R_0 = 396.6$MPa, $R_\infty = 471.5$MPa, $b = 8$, $C = 7500$MPa, $\gamma = 70$.

On the other hand, the formulation of the PB model does not separate the cyclic hardening or softening effect due to plastic deformation from the softening effect induced by damage evolution. The parameters were therefore tuned to reproduce the softening behaviour recorded experimentally. The results covering all of the strain

ranges tested are R_0 = 429.0MPa, R_∞ = 387.5MPa, b = 0.1141, C = 11431MPa, γ = 128.9 (see Figs. 9a-b).

4.2 LPD model parameters

The calibration was made with the objective to match the instant at which specimen´s failure was recorded during tensile tests on RBs. A trial-and-error procedure was used to meet the failure points, see also Bernauer and Brocks (2002). Since the number of model parameters is quite high, the choice was restricted based on the following considerations:

i) The factors q_i (i = 1-3) in the yield function were set to the well established values, that is q_1 = 1.5, q_2 = 1.0, $q_3 = q_1^2$ = 2.25.

ii) Void nucleation was not accounted for by setting f_N = 0. This is justified by the fact that this kind of steels typically contains a high fraction of weakly bonded MnS inclusions which act as void nucleation sites as soon as the yield stress is exceeded (Decamp *et al.* (1997)). The growth of such voids is then the prevailing damage mechanism.

FE simulations of both 5 and 10mm diameter RBs were performed using isotropic hardening only with material behaviour calculated from tensile tests. A satisfying fit of experiments was found with f_0 = 0.01, f_c = 0.07, κ = 4.0.

4.3 PB model parameters

The parameters α, D_{cr}, D_0, ε_f, ε_{th} of the PB model employed here were evaluated by fitting the results of tests on FRHG specimens from which the damage was evaluated from the decrease of stiffness, i.e. $D = 1 - E/E_0$, and plotted as a function of plastic strain (Fig. 10). The damage accumulates fast in the early plastic deformation stage, showing an almost stepwise trend because of the presence of weakly bonded MnS inclusions. This behaviour has therefore been approximated by assuming an initial damage D_0 = 0.15 and a threshold strain ε_{th} = 0.0213. The best fit was finally obtained with the set: α = 0.362, D_{cr} = 1, D_0 = 0.15, ε_{cr} = 1.5, ε_{th} = 0.0213. From Fig. 6 a failure strain ε_f of about 1.2 can be inferred. A value of 1.5 of the critical strain ε_{cr} in the damage model is therefore justified since failure in tensile tests on RB occurred after a prominent necking phase, where a higher triaxiality and hence damage rate, develops. Further details on parameters calibration can be found in Bonora et al. (2004).

The minimum requirement for model and parameter validation is that failure under tensile loading of different specimens can be correctly predicted. Therefore, tensile tests on RB have been compared with corresponding FE simulations with the PB model. The results are summarized in Fig 11, where it is shown that the instant of failure simulated falls within range found experimentally. In the case of the LPD model, this particular comparison is redundant, as the damage parameters have been calibrated using the tests on RBs.

5. LIFETIME PREDICTIONS

Leblond-Perrin-Devaux (LPD) model. Predictions of the cyclic plastic behaviour of RNBs were carried out and compared with the respective tests. For the sake of conciseness, only one test of a RNB with 2 mm notch radius and one with 10 mm notch radius were chosen for the comparison. The tests were run under a displacement range of ±0.1 mm in case of the sharp notch, ±0.2 mm in case of the smooth notch. For this

particular choice, the average plastic strain accumulation per cycle on the minimum section of the specimen varies in from 1.5% to 5%, depending on notch radius and position (centre or notch root). The test specimens showed a macrocrack after 83 (RNB2) and 40 cycles (RNB10), respectively. At this stage, the tests were stopped to be able to perform metallographic inspection. Figure 12 depicts the macroscopic cyclic force-displacement behaviour of the two bars. Generally, for both specimen geometries, the resulting force is increasing in the first load cycles, followed by a number of stable loops. Initiation of a macroscopic crack is preceded by a fast decrease in maximum load.

For a better understanding of both, experimental and simulation results, the following representation related to cyclic stress-strain-curves is used. For each cycle, maximum and minimum loads are recorded and plotted as a function of the number of cycles, see figures 13 and 14. Generally, the fundamental features in macroscopic behaviour can be caught in the simulation: hardening during the first cycles, followed by a decrease of maximum and minimum load due to increasing damage. The difference between tensile and compressive peak loads is due initially to contraction-expansion of the cross-section, later it is amplified by increasing degradation and damage. However, using the model parameters calibrated by tensile tests on RBs, the predicted lifetime is too high. This is manifested by the two curves in figures 13 and 14 labelled "#1", showing almost constant loads from the 20^{th} cycle on. Obviously, damage evolution is too weak to cause a sufficient decrease of the peak loads.

The prediction can be improved be the introduction of the strain controlled void nucleation, Eqn. (11). The curves in figures 13 and 14 labelled "#2" are obtained by simulations using the parameters $f_0 = 0.005, f_c = 0.2, \kappa = 2.0, f_N = 0.08, \varepsilon_N = 3.0, s_N = 1.0$. The predicted lifetime for the RNB2 is the same as in the experiment, for RNB10 failure occurs in the 23^{rd} cycle. On the other hand, the improvement in cyclic life prediction obtained with set "#2" occurred at the expense of the displacement to failure in the simulation of RB tests, which is about 15% lower than with set "#1".

An interesting feature of the simulations explains the different consequences with respect to the global specimen behavior. The simulations of RNB2 using the parameter set #1 showed an accumulation of f^*at the centre of the notched section, whereas cracking in the experiments starts at the specimens surface. The introduction of the nucleation term, which is sensitive to plastic strain, allows to displace the "damage hot spot" towards the notch root, where failure is detected to begin experimentally. In the case of 2 mm notch radius, the strain concentration obtained in the FE analysis is strong enough to promote failure at the notch root, see fig. 15a. The corresponding evolution of the damage variable at two different loci in the specimen, namely the middle and the notch root, are displayed in fig. 16. Note, that while using parameter set #2 in the case of the sharp notch, damage is generally higher in the notch root compared to the specimen´s centre. For 10 mm notch radius, however, the locus of maximum damage remains in the specimen´s center, see fig. 15b. For this type of specimen, triaxiality and plastic strain are maximum in the centre of the specimen, and therefore damage accumulates at this position, see fig. 16. Exact prediction of the number of cycles to failure could not be achieved for both notched specimens tested. Despite the fact that for the smooth notched bar the number of cycles is underpredicted, the simulation using parameter set #2 captures the specimens' macroscopic and microscopic response. As experimental results with respect to fatigue life generally show a large scatter, it is not substantial to meet the exact number for one distinct test. More interesting, however, is

the fact that the maximum loads are not met and this holds for both damage models envisaged here, LPD and PB (see following section). A reason for this can be found in tha fact that strains in the RNB cross section spans from 1.5 to 5% while the material behaviour parameters were tuned on DLC experimentson a range from 1.5 to 2.5%.

Pirondi-Bonora (PB) model. According to this model, damage manifests its effects with a decrease of stiffness. In Fig. 17 the experimental and simulated load-displacement cycles are shown. The number of cycles represented corresponds to: i) in the simulations, the point at which convergence is lost due to attainment of critical damage; ii) in the experiments, the point at which a macrocrack manifests at the surface. It can be noticed also that the stiffness change is not active while reloading from compression and, in the case of 10mm notch radius, softening is recovered upon a certain negative displacement, that is when all the elements along the cross section recover the load carrying capability according to Eqn. (25). While the overall behaviour is matched, the decrease of stiffness is quite overestimated. A damage rate larger then the LPD model could be expected since in this case there is not a negative damage rate associated with a compressive state of stress and the effect of hydrostatic stress relaxation due to porosity is not present. This fact of course is reflected by the predicted lifetimes. In the case of the 2mm notch radius, about 30 cycles are needed to inititiate a crack in the experiments, while the prediction is 12. In the lower triaxiality case, i.e. 10mm notch radius, the FE prediction is 22 cycles to failure, while experimentally it was greater than 100 cycles.
An explanation can be found by examining the damage distribution at mesocrack initiation, i.e. when the first element reaches D_{cr} at all of the integration points, Fig. 18. In the case of the 2mm notch radius the critical damage point is localized just beneath the notch root. In this case, the higher plastic strain accumulation at the notch root prevails on the higher triaxiality at the centre, as found also in Pirondi and Bonora (2003). On the other hand, in the lower triaxiality geometry (10mm radius) damage is always localized at the centre, since plastic strain is fairly constant across the section. It seems therefore that the acceleration imparted by the triaxiality in the model is in this case too strong with respect to the experimental evidence.

Comparison of LPD and PB models. The two models are compared in terms of the predicted degradation of mechanical properties. The mechanical properties to be monitored were chosen according to the way damage exploits its effects in the two models. In the case of LPD an increase of the void volume fraction causes the shrinkage of the yield surface and in turn the reduction of the load with respect to the undamaged condition, while an increase of damage in PB reduces the elastic modulus, hence the global stiffness of the specimen. Therefore, peak load, P_{max}, and global (elastic) stiffness, $K=dP/d(\Delta l)$, were determined as a function of the number of cycles, N, for LPD and PB, respectively. The superscripts '+' and '-' indicate values taken on the tensile and compressive parts of the cycle, respectively. To compare the results, P_{max} and K were normalized with respect to the reference (undamaged) values. The reference value of peak load was identified as the maximum one recorded, neglecting the damage accumulated so far. Anyway since the initial increase of peak load is very rapid this was considered as a good approximation. As far as the concern is to compare the way damage accumulates during the experimental or predicted lifetime and not its time (or strain) evolution, the number of cycles can also be normalized for experimental and

simulated values by the experimental, N_f, and simulated, $N_{f\text{-}FEM}$, numbers of cycles to failure, respectively.
The results are shown in Figs. 19 (LPD) and 20 (PB). The LPD model predicts a smoother degradation than the PB model except close to failure, where there is an abrupt change in the degradation trend. Both models give a lower, if null, degradation under compression, that is qualitatively in agreement with the experiments. Finally, the LPD model predicts generally a degradation lower than the experiment, while the situation is the opposite for the PB model.

Metallographic inspection. A metallographic inspection was conducted after testing to check for the development of damage along the cross section of the specimens. One specimen for each notch radius was sectioned longitudinally. Both specimens were subjected to a +/- 0.1mm displacement cycles. The experiments were stopped prior to final failure of the respective specimens. The section of the 2mm notch radius specimen shows a macrocrack already initiated at the notch root (Fig. 21). This macrocrack is surrounded by a number of voids originating from inclusions. Cracks developing from inclusions ahead of the notch root are also visible. On the other hand, any instance of this kind was not found in the centre of the specimen, in agreement with the prediction of the two models of a lower level of damage at this location (see Figs. 15 and 18).
A sectioned 10mm notch radius specimen is shown in Fig. 22. Macrocracks did not yet develop in this case but, differently from the sharper notched specimen, coalescence of voids started from broken particles could be detected both at notch root and centre. The reason for this is of course the more uniform strain distribution with respect to the 2mm notch radius case. The small strain concentration at the root is probably compensated, from the point of view of the damage mechanism, by a slightly higher stress triaxiality at the centre. A higher damage concentration at the centre, as predicted by both the models, could not be found at least at this stage of the failure process.

6. CONCLUSIONS

Two different micromechanical models based on either porosity evolution (LPD model) or CDM (PB model), respectively, have been used to simulate macroscopic response and local damage evolution of RNB specimens subjected to cyclic plastic loading.
The predictions of the models agreed with the experiments to a different extent depending on the variable considered for the comparison and on the notch radius (i.e level of triaxiality) of the specimen. In particular, with the help of a strong nucleation rate the LPD model can match the number of cycles to failure better than the PB model, which tend to overestimate the damage rate and, therefore predict lifes shorter than the experiments. On the other hand, at least for the higher triaxiality/cyclic plastic strain case (2mm notch radius), the PB model indicated failure location at the notch root, which is in agreement with the one detected experimentally. The LPD model instead, predicts always the failure to start at the interior of the specimen.
The models have therefore to be improved to simulate properly all of the conditions considered. The work will be therefore extended to the investigation of the damage micromechanism in relationship with the evolution of damage indicators, such as porosity, elastic modulus and cyclic stress range.

REFERENCES

McClintock, F.A., A criterion for ductile fracture by the growth of holes, *J. of Applied Mechanics*, 1968, **35**, 363-371.

Rice, J. R. and Tracey, D. M. (1969). On the ductile enlargement of voids in triaxial stress fields. J. Mech. Phys. Solids **17**, 201-217.

Gurson, A. L. (1977). Continuum theory of ductile rupture by void nucleation and growth: Part I - yield criteria and flow rules for porous ductile media. J. Eng. Mater. Technol.-Trans. ASME **99**, 2-15.

Needleman, A. and Rice, J. R. Limits to ductility set by plastic flow localization. D. P. Koistinen. Mechanics of sheet metal forming. 237-78. New York, Plenum Press.

Needleman, A. and Tvergaard, V. (1984). An analysis of ductile rupture in notched bars. J. Mech. Phys. Solids **32**, 461-490.

Rousselier, G. (1987). Ductile fracture models and their potential in local approach of fracture. Nucl. Eng. Design **105**, 97-111.

Tvergaard, V. and Niordson, C., 2004. Non local plasticity effects on interaction of different size voids, International Journal of Plasticity, **20**, pp. 107-120.

Acharya, A., Bassani, J.L., 2000. Lattice incompatibility and a gradient theory of crystal plasticity. Journal of the Mechanics Physics of Solids, **48**, 1565–1595.

J. Wen, Y. Huang, K. C. Hwang, C. Liu and M. Li (2005). The modified Gurson model accounting for the void size effect, International Journal of Plasticity, **21**, 381-395.

Zhenhuan Li and Minsheng Huang (2005). Combined effects of void shape and void size– oblate spheroidal microvoid embedded in infinite non-linear solid, International Journal of Plasticity, **21**, 625-650.

Minsheng Huang and Zhenhuan Li (2005). Size effects on stress concentration induced by a prolate ellipsoidal particle and void nucleation mechanism, International Journal of Plasticity, **21**, 1568-1590.

Schacht, T., Untermann, N., and Steck, E., 2003. The influence of crystallographic orientation on the deformation behavior of single crystals containing microvoids, International Journal of Plasticity, **19**, 1605-1626

Bonfoh., N., Lipinski, P., Carmasol, A., and Tiem, S., 2004. Micromechanical modeling of ductile damage of polycrystalline materials with heterogeneous particles, International Journal of Plasticity, **20**, pp. 85-106.

Xia, L. and Shih, C.F., 1995. Ductile Crack Growth-I. A numerical study using computational cells with microstructurally-based length scales, J. Mech. Phys. Solids, **43**, (2), pp. 233-259.

Brocks, W.; Hao, S., and Steglich, D. Micromechanical modelling of the damage and toughness behaviour of nodular cast iron. Journal De Physique III. 1996; 6(colloque C6):43-56.

Mahnken, R., 2002. Theoretical, numerical and identification aspects of a new model class for ductile damage, International Journal of Plasticity, **18**, pp.801-831.

Besson, J., Steglich, D., and Brocks, W., 2003. Modeling of plane strain ductile rupture, International Journal of Plasticity, **19**, pp. 1517-1541.

Negre, P.; Steglich, D., and Brocks, W. Crack extension in aluminium welds: a numerical approach using the Gurson-Tvergaard-Needleman model. Eng. Fract. Mech. 2004; 71(16-17):2365-2383.

Huang Yuan and Jian Chen, (2004). Comparison of computational predictions of material failure using nonlocal damage models, International Journal of Solids and Structures, **41**, 1021-1037.

Lemaitre, J. (1985). A continuous damage mechanics model for ductile fracture. Journal of Engineering Materials and Technology **107**, 83-89.
Chandrakanth, S. and Pandey, P. C. (1993). A new ductile damage evolution model. Int. J. Fracture **60**, R73-R76.
Bonora, N., (1997a). A Non-Linear CDM Model for Ductile Failure, Engineering Fracture Mechanics **58**, 11-28
Bonora, N. (1997b). On the effect of triaxial state of stress on ductility using nonlinear CDM model, International Journal of Fracture **88**, 359-371.
Tai, H.W., and Yang, B.X., 1986. A new microvoid-damage model for ductile fracture, Engn. Frac. Mech., **25**, (3), pp. 377-384.
Tai, H.W., 1990. Plastic damage and ductile fracture in mild steels, Engineering Fracture Mechanics, **36**, (4), pp. 853-880.
Z. Lin, C. Lingcang, L. Yinglei, P. Jianxiang, J. Fuqian and C. Dongquan, (2004). Simplified model for prediction of dynamic damage and fracture of ductile materials, International Journal of Solids and Structures, **41**, 7063-7074.
N. Bonora, D. Gentile, A. Pirondi and G. Newaz (2005). Ductile damage evolution under triaxial state of stress: theory and experiments, International Journal of Plasticity, **21**, 981-1007
Fleck, N.A., Hutchinson, J.W., 1997. Strain gradient plasticity. Adv. Appl. Mech., **33**, 295–361.
Fleck, N.A., Muller, G.M., Ashby, M.F., Hutchinson, J.W., 1994. Strain gradient plasticity: theory and experiment, Acta Metallurgica et Materialia, **42**, 475–487.
Bammann, D.J., Mosher, D., Hughes, D.A., Moody, N.R., Dawson, P.R., 1999. Using spatial gradients to model localization phenomena. Sandia National Laboratories Report, SAND99- 8588, Albuquerque, New Mexico 87185 and Livermore, CA.
Brünig, M., 2003. An anisotropic ductile damage model based on irreversible thermodynamics, International Journal of Plasticity, **19**, pp.1679-1713.
Michael Brünig and Sabine Ricci, (2005). Nonlocal continuum theory of anisotropically damaged metals, International Journal of Plasticity, **21**, 1346-1382.
A. Menzel, M. Ekh, K. Runesson and P. Steinmann (2005). A framework for multiplicative elastoplasticity with kinematic hardening coupled to anisotropic damage, International Journal of Plasticity, **21**, 397-434.
Voyidajis, G., Abu Al-Arub, R.K., Palazzotto, A. N., 2004. Thermodynamic framework for coupling of non-local viscoplasticity and non-local anisotropic viscodamage for dynamic localization problems using gradient theory, International Journal of Plasticity, **20**, pp.981-1038.
Lammer, H., and Tsamakis, Ch. (2000). Discussion of coupled elastoplasticity and damage constitutive equations for small and finite deformations, International Journal of Plasticity, **16**, 495-523.
Klesnil, M., Lukaš, P. (1980). Fatigue of metallic materials, Elsevier Science Publishers, Amsterdam.
Polak, J. (1991), Cyclic plasticity and low cycle fatigue of metals. Elsevier Science Publishers, Amsterdam.
Leblond, J.-B., Perrin, G., and Devaux, J. (1995). An improved Gurson-type model for hardenable ductile metals. Eur. J. Mech. A-Solids **14**, 499-527.
Besson, J. and Guillemer-Neel, C. (2003). An extension of the Green and Gurson models to kinematic hardening. Mechanics of Materials **35**, 1-18.
Cedergren, J., Melin, S. and Lidström, P. (2004). Numerical modelling of P/M steel bars

subjected to fatigue loading using an extended Gurson model, European Journal of Mechanics A/Solids **23**, 899-908.
Pirondi, A. and Bonora, N. (2003). Modeling ductile damage under fully reversed cycling, Computational Materials Science **26**, 129–141.
Xiao, Y. (2004). A multi-mechanism damage coupling model, International Journal of Fatigue **26**, 1241-1250.
Yang, X. and Nassar, S. (2005). Constitutive modelling of time-dependent cyclic straining for solder alloy 63Sn-37Pb, Mechanics of Materials, **37**, 801-814.
Gomez, J. and Basaran, C. (2005). A thermodynamics based damage mechanics constitutive model for low cycle fatigue analysis of microelectronics solder joints incorporating size effects, International Journal of Solids and Structures, **42**, 3744-3772.
Bernauer, G. and Brocks, W. (2002). Micro-Mechanical Modelling of Ductile Damage and Tearing - Results of a European Numerical Round Robin. Fatigue Fract. Eng. Mater. Struct. **25**, 363-384.
Bonora, N., Gentile, D. and Pirondi, A. (2004). Identification of the parameters of a non-linear continuum damage mechanics model for ductile failure in metals, Journal of Strain Analysis for Engineering Design **39**, 639-651.
Lemaitre, J. (1996). A Course on Damage Mechanics, Springer-Verlag, Berlin.
Hughes T.J.R., Winget J. (1980). Finite Rotation Effects in Numerical Integration of Rate Constitutive Equations Arising in Large - Deformation Analysis. Int. J. Num. Meth. Engng **15**, 1862-1867.
Aravas, N. (1987). On the numerical integration of a class of pressure-dependent plasticity models. Int. J. Num. Meth. Engng. **24**, 1395-1416.
Chu, C. C. and Needleman, A. (1980). Void nucleation effects in biaxially stretched sheets. J. Eng. Mater. Technol.-Trans. ASME **102**, 249-256.
Tvergaard, V. and Needleman, A. (1984). Analysis of the cup-cone fracture in a round tensile bar. Acta metall. **32**, 157-169.
Mühlich, U. and Brocks, W. (2003). On the numerical integration of a class of pressure-dependent plasticity models including kinematic hardening. Comp. Mech. **31**, 479-488.
Chaboche, J. L. (1989). Constitutive equations for cyclic plasticity and cyclic viscoplasticity. Int. J. Plast. **5**, 247-302.
Bonora, N., Gentile, D. and Iacoviello, F., (1996). Triassialità e rottura duttile in provini cilindrici con intaglio circonferenziale, Proceedings of XII Italian Group of Fracture Annual Conference - IGF12, Parma, June, pp. 93-102.
Pugh H.Ll.D. (1970). The Mechanical Behavior of Materials Under Pressure, Elsevier Science Publishers, 1970.
Decamp, K., Bauvineau, L., Besson, J., Pineau, A., (1997). Size and geometry effect on ductile rupture of notched bars in a C-Mn steel : experiments and modelling. Int. J. Fract. **88,** 1–18.
Steglich, D.; Pirondi, A.; Bonora, N., and Brocks, W. (2005). Micromechanical modelling of cyclic plasticity incorporating damage. Int. J. Solids Struct., **42**, 337-351.

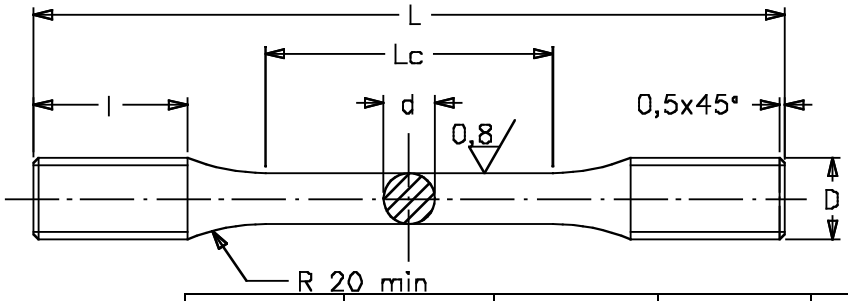

d [mm]	L [mm]	L_c [mm]	D	l [mm]
5	73.2	28	M8	15
10	146.4	56	M16	30

Fig. 1: RB specimen for tensile testing.

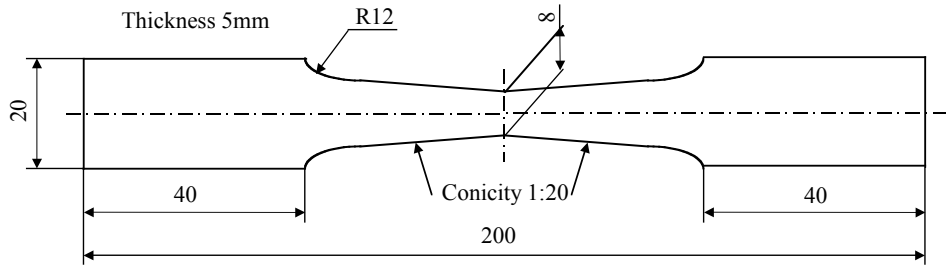

Fig. 2: FRHG specimen geometry and dimensions

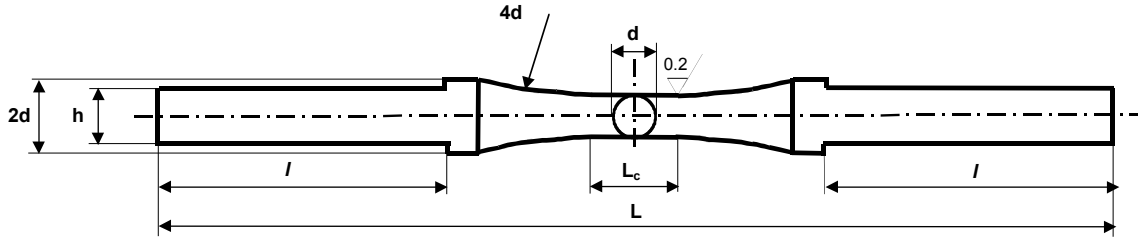

d [mm]	L [mm]	L_c [mm]	h	l [mm]
6.5	140	10	10	50

Fig. 3: DLC specimen for strain-controlled cyclic plasticity testing.

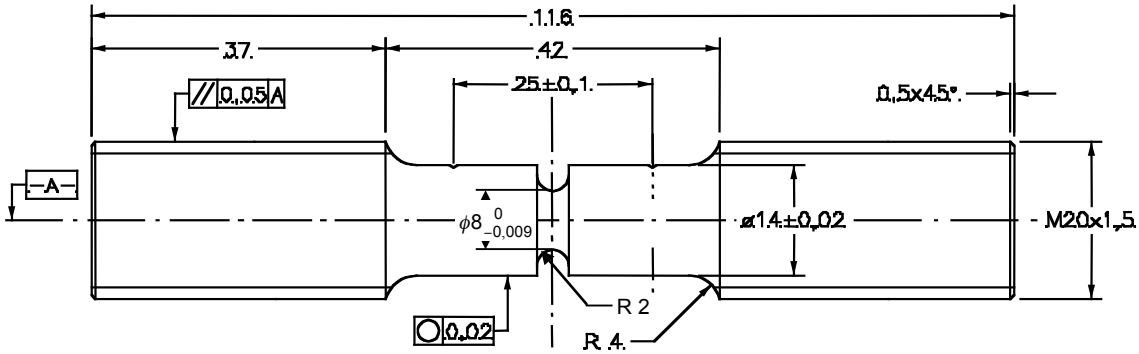

Fig. 4: RNB2 specimen geometry and dimensions

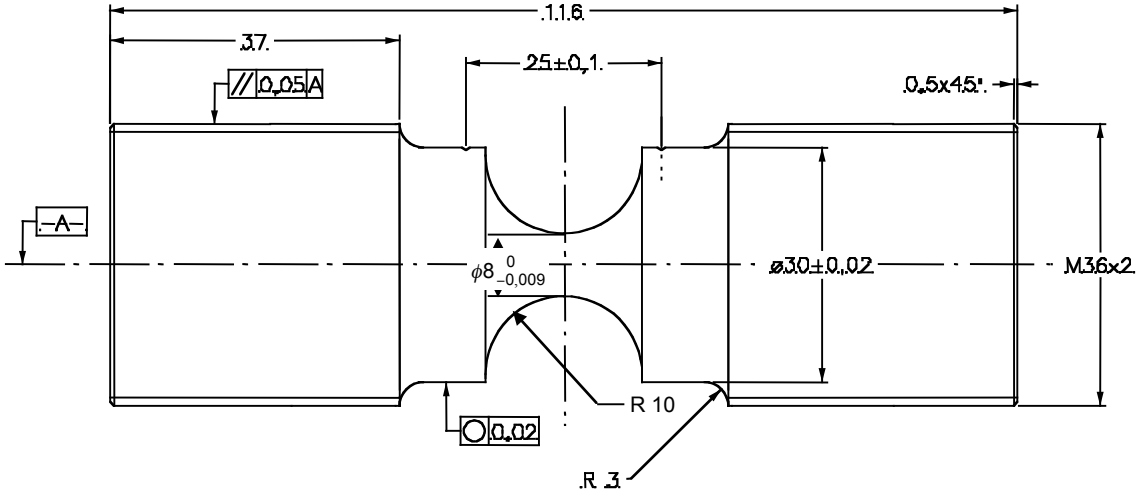

Fig. 5: RNB10 specimen geometry and dimensions.

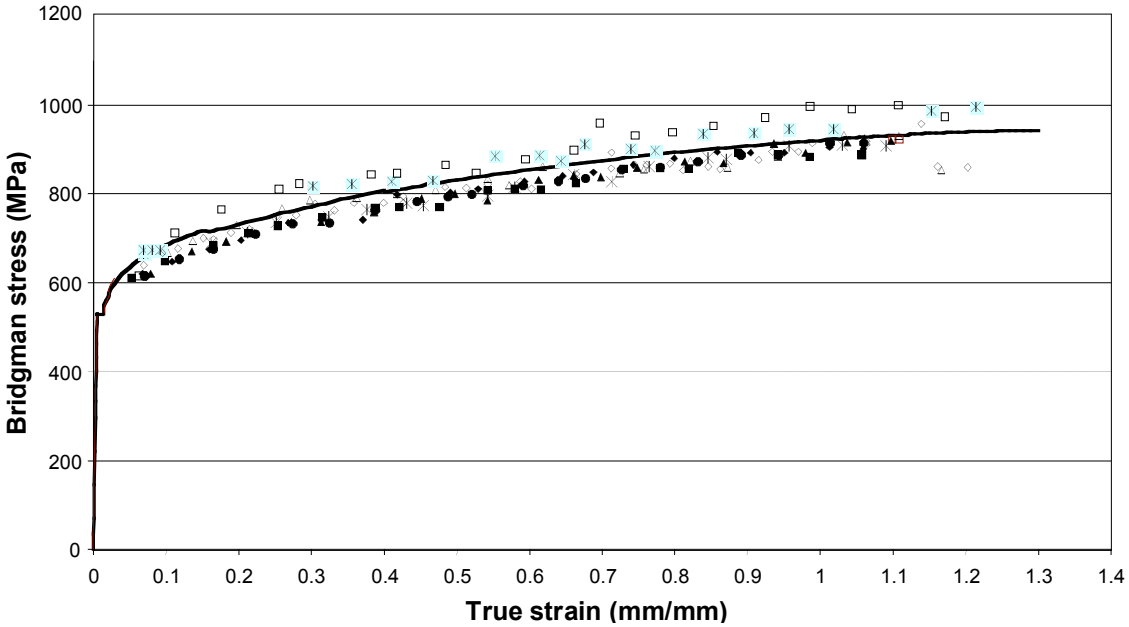

Fig. 6: Bridgman stress-true strain experimental data (all specimens) and curve fit.

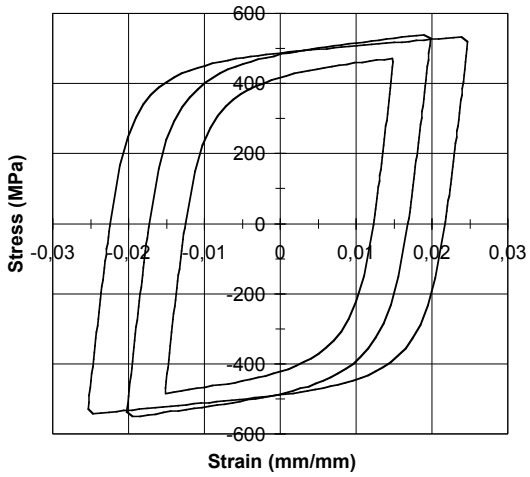

Fig.7: stabilized cycles for different strain amplitudes.

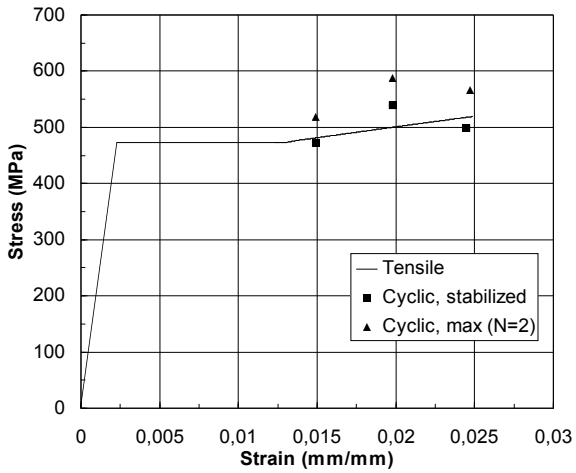

Fig. 8: cyclic vs. tensile behaviour.

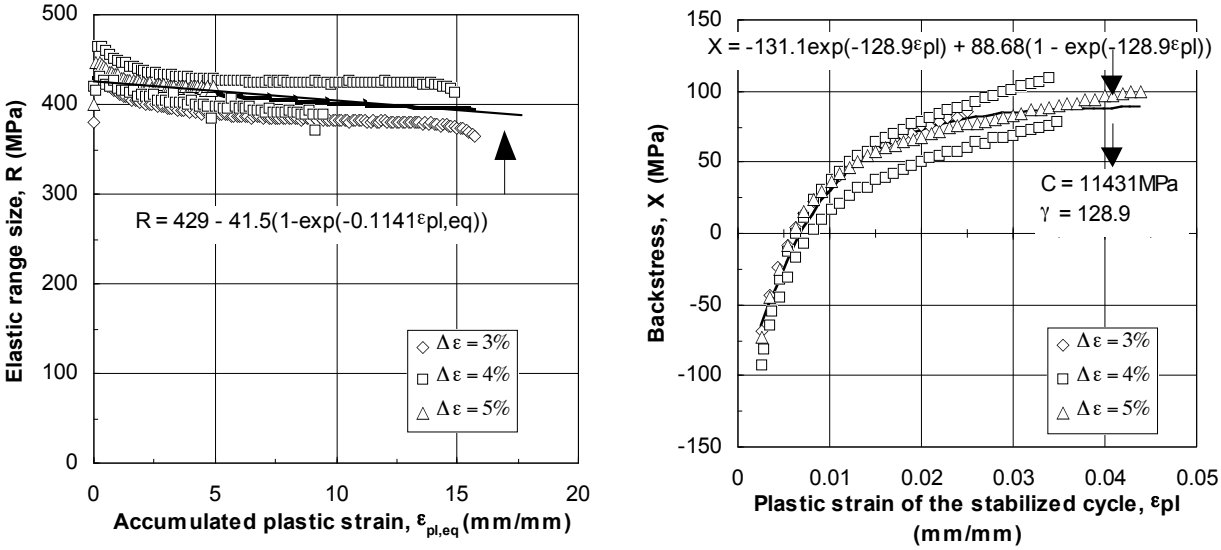

(a) (b)

Fig. 9: a)evolution of the elastic range size as function of accumulated plastic strain.; b) backstress evolution during a cycle after stabilization

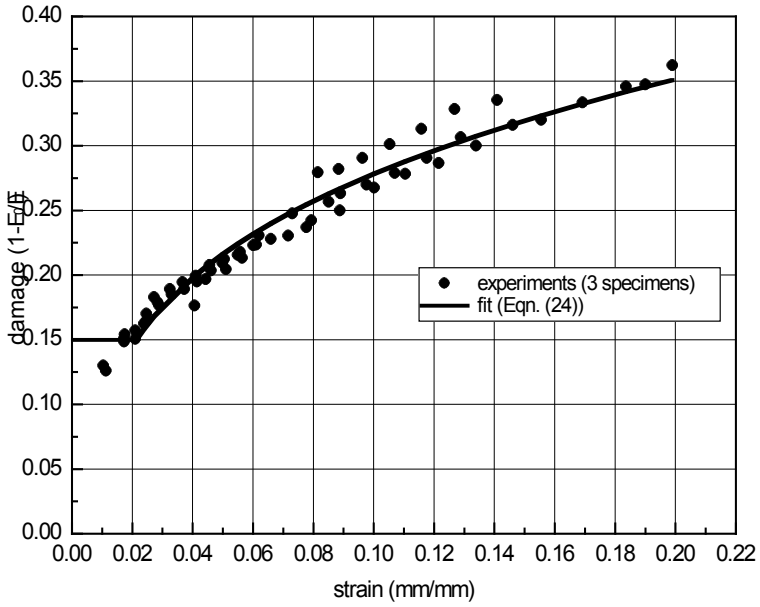

Fig. 10: evolution of damage as a function of plastic strain.

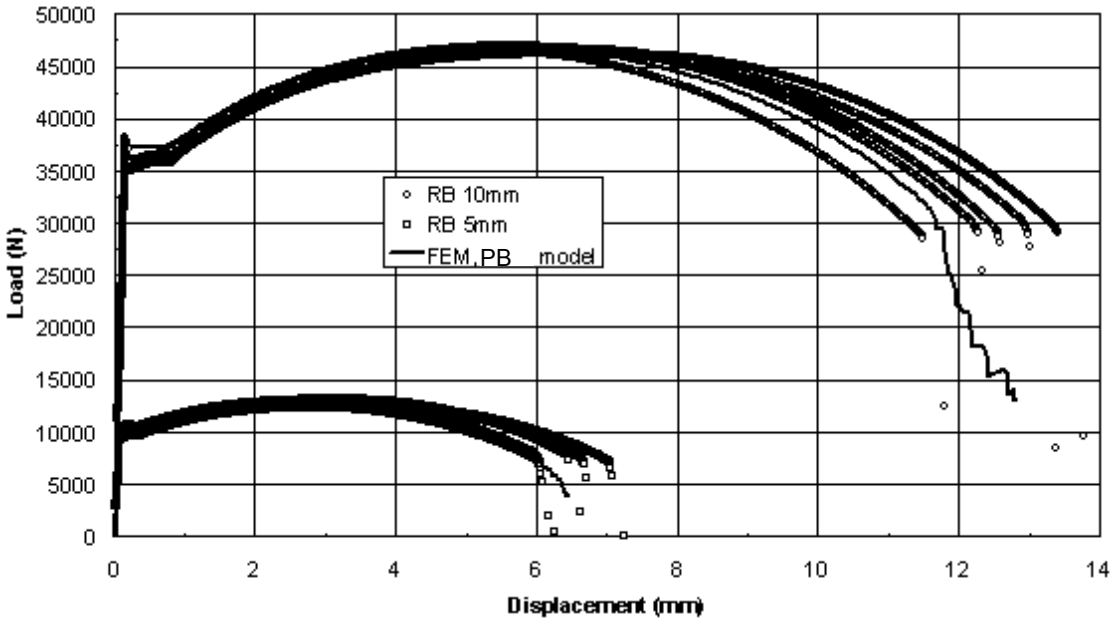

Fig. 11: comparison between RB tensile tests and prediction of the PB model.

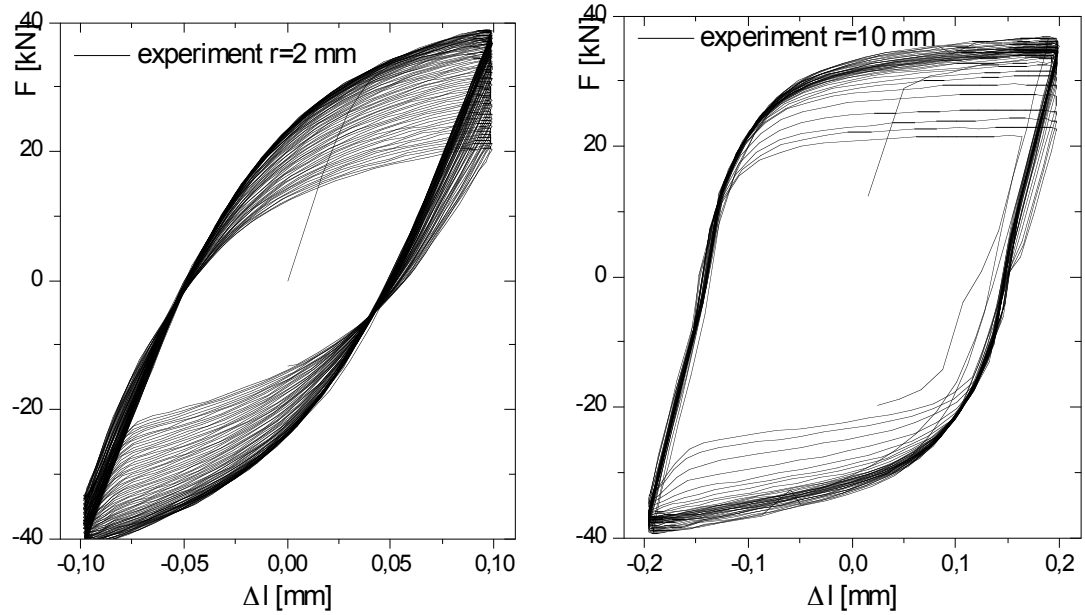

(a) (b)

Fig. 12. experimental load-displacement cycles taken for (a) RNB2 and (b) RNB10.

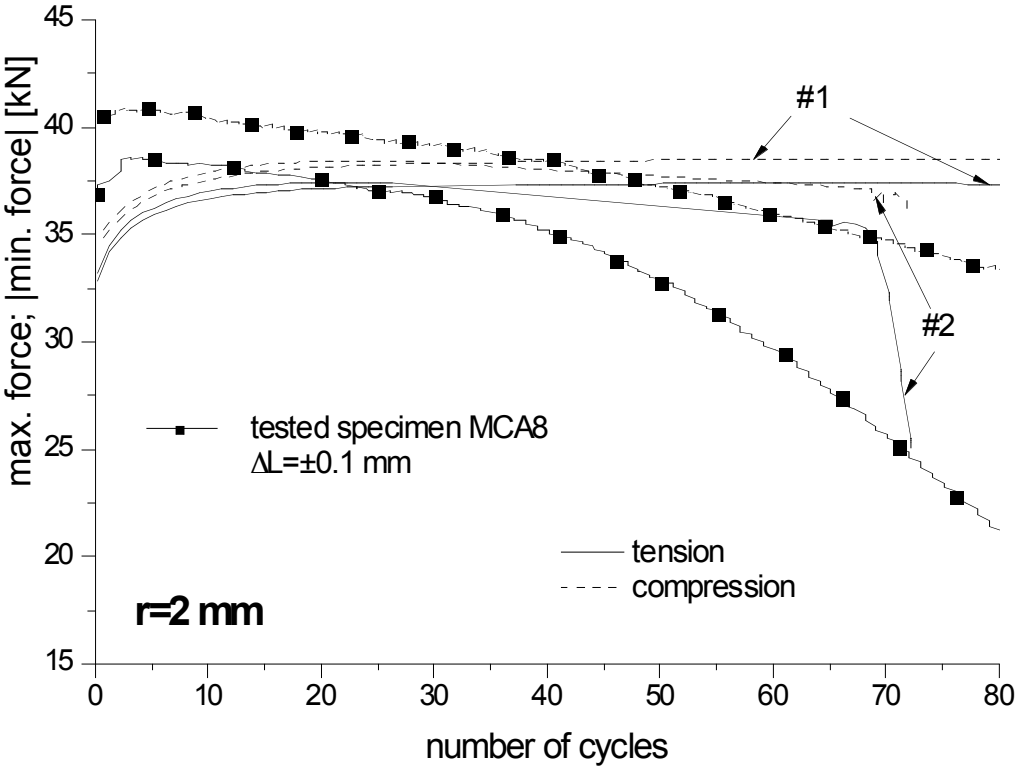

Fig. 13. evolution of peak load in tension and compression of RNB2 as a function of the loading cycles (LPD model).

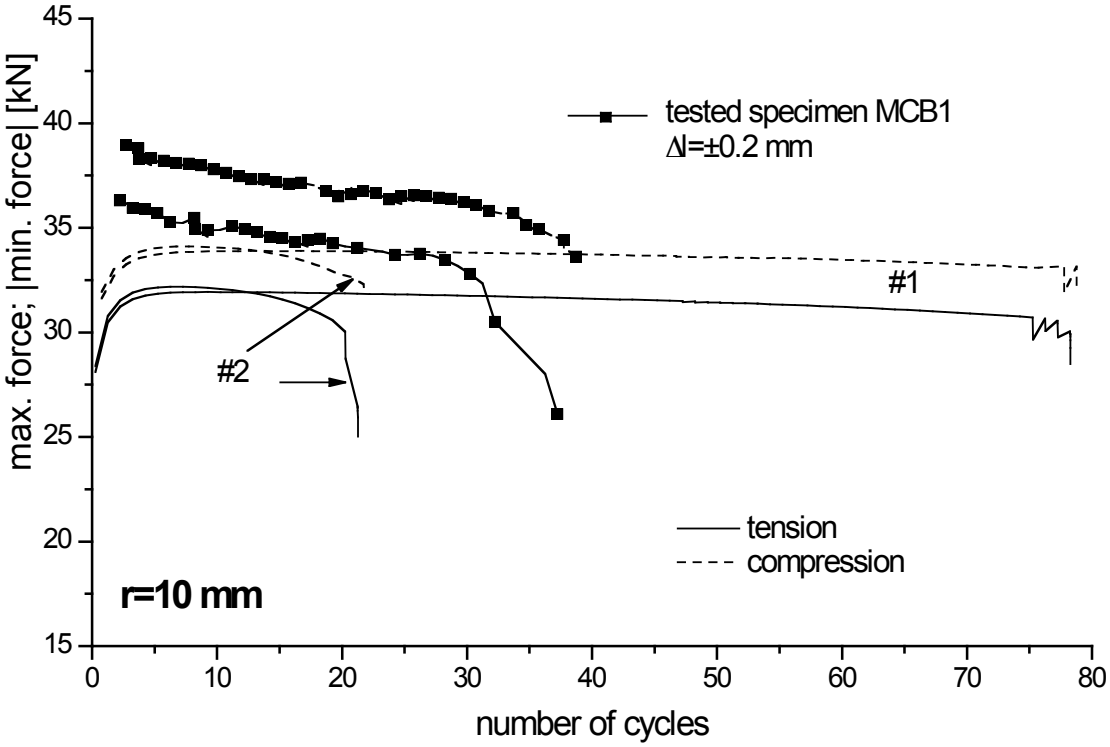

Fig. 14. evolution of peak load in tension and compression of RNB10 as a function of the loading cycles (LPD model).

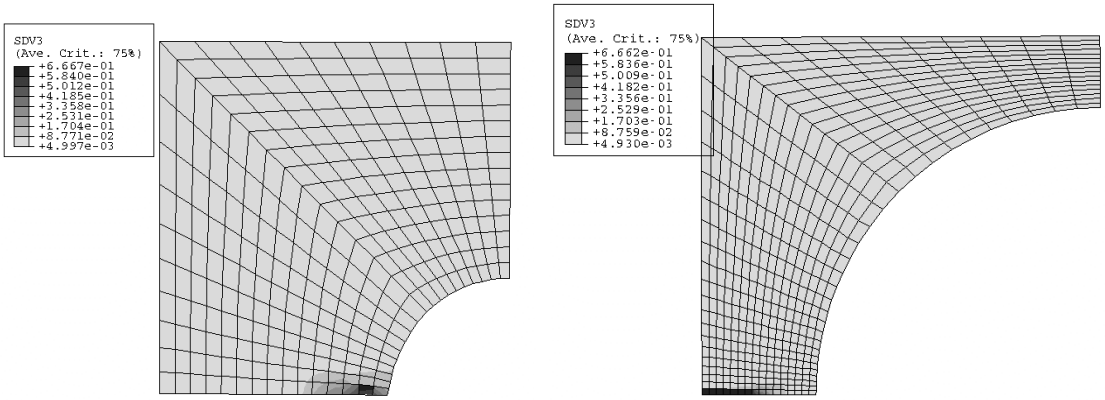

(a) (b)

Fig. 15. contours of constant damage variable, *f**, in (a) RNB2 and (b) RNB10 at failure

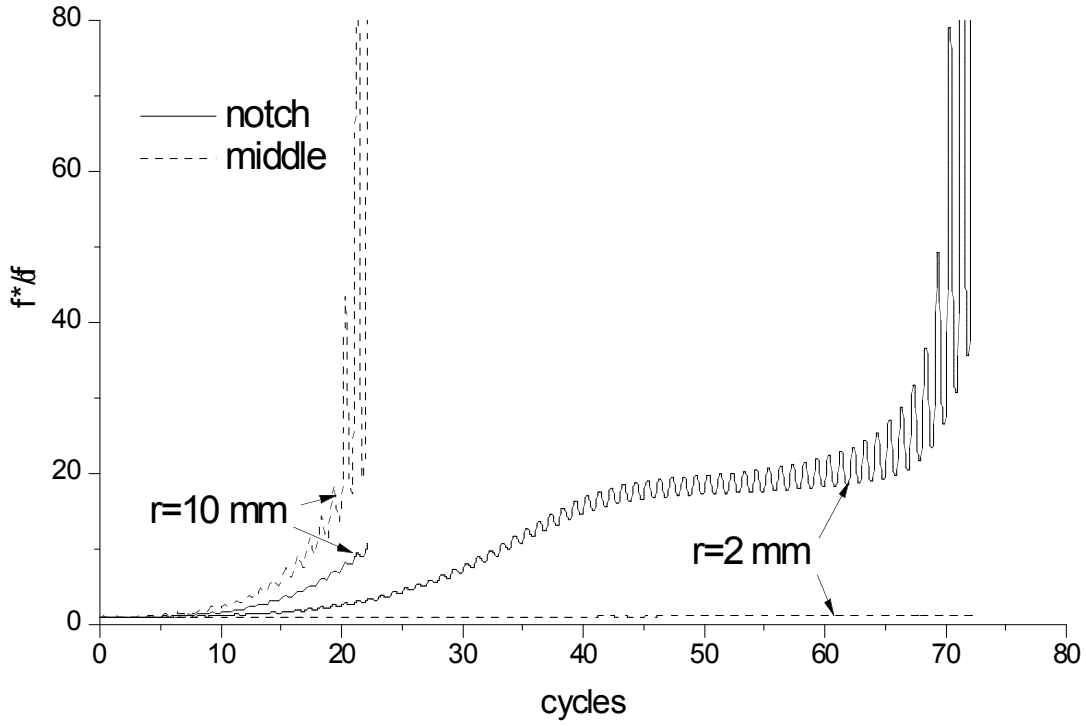

Fig. 16. evolution damage variable, *f**, near the specimen surface at the notch and in the middle of the specimen for the two geometries envisaged

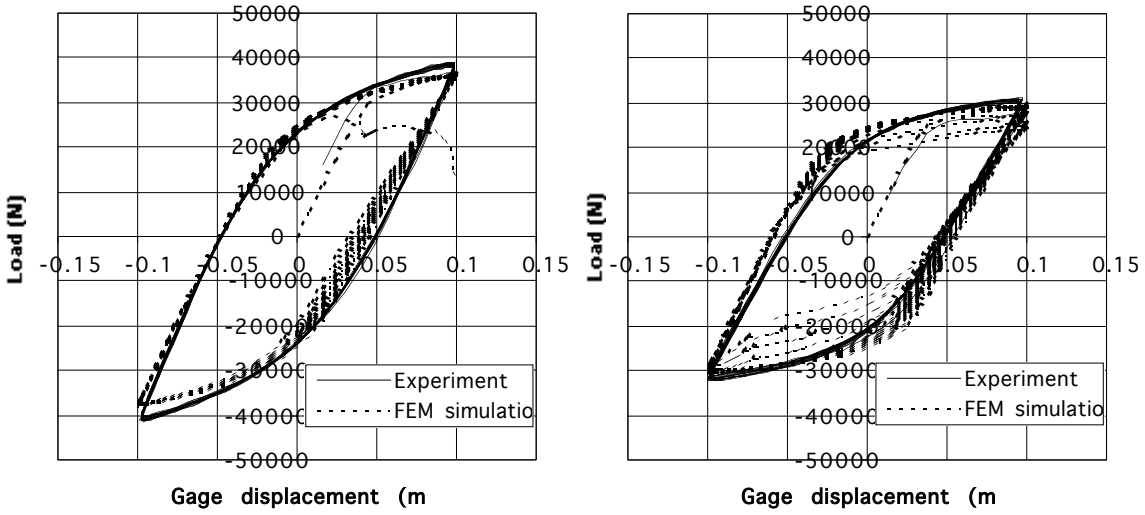

(a) (b)

Fig. 17: experimental vs. simulated load-displacement cycle with the PB model: a) RNB2; b) RNB10.

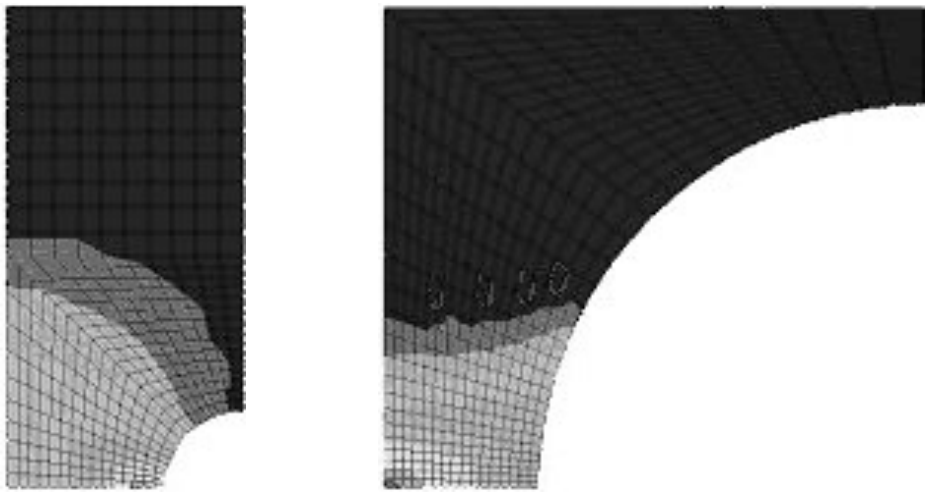

(a) (b)

Fig. 18: predicted distribution of damage *D* at mesocrack initiation: a) RNB2; b) RNB10.

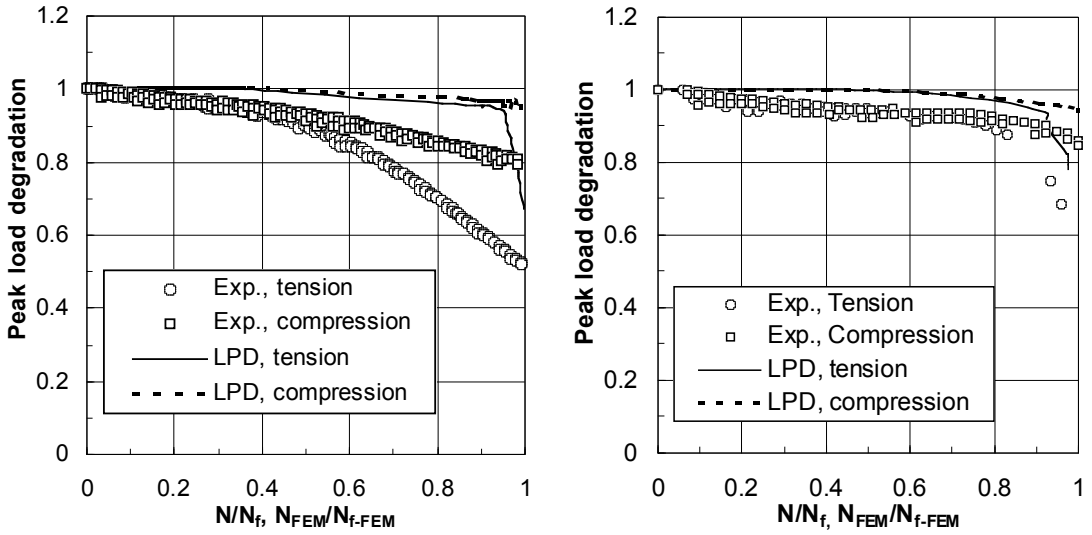

(a) (b)

Fig. 19: experimental and LPD-predicted peak load degradation: a) RNB2; b) RNB10.

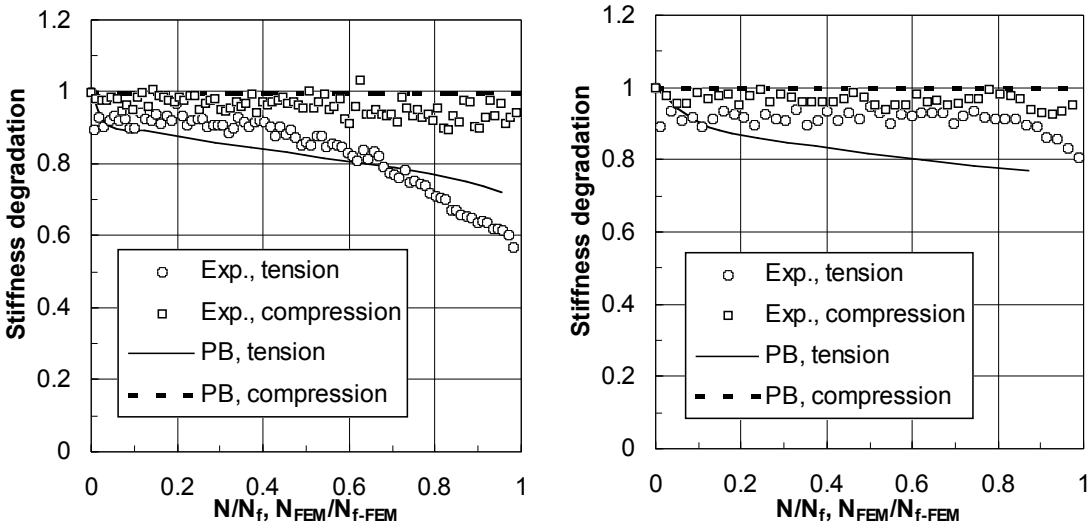

(a) (b)

Fig. 20: experimental and PB-predicted stiffness degradation: a) RNB2; b) RNB10.

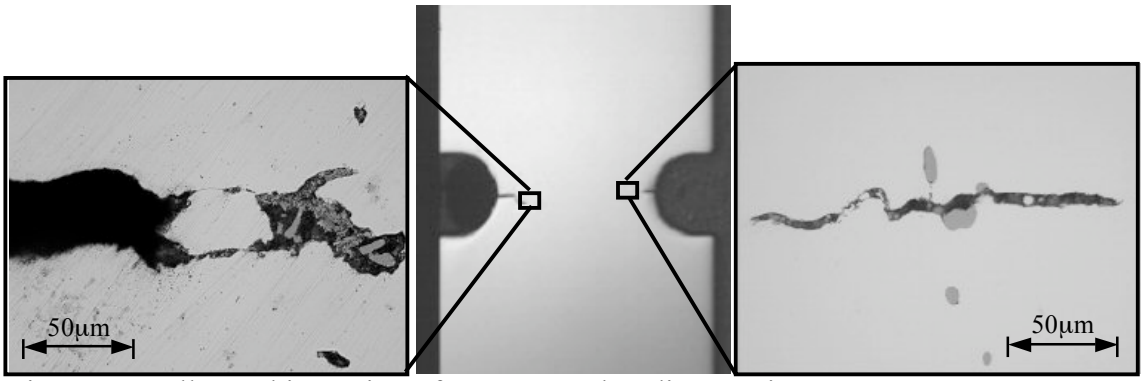

Fig. 21: metallographic section of a 2mm notch radius specimen.

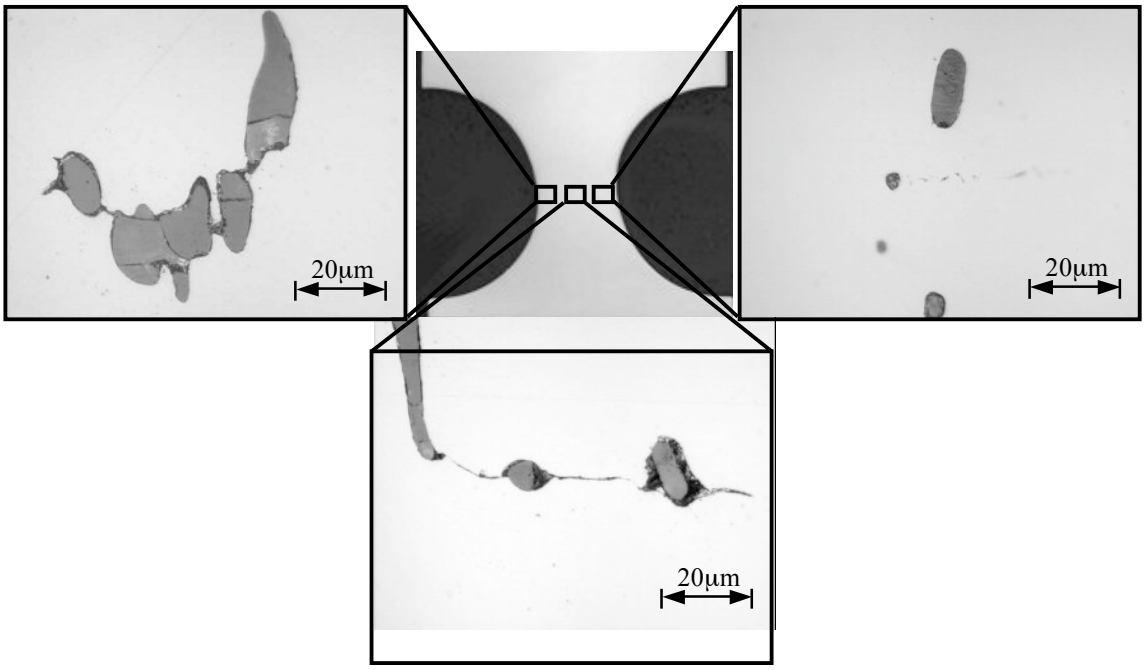

Fig. 22: metallographic section of a 2mm notch radius specimen.

Table 1 - Material composition for 20MnMoNi55 steel.

C	Si	Mn	P	S	Cr	Mo	Ni	Cu
0.19	0.2	1.29	0.007	0.008	0.12	0.53	0.8	0.11